

Article

Development and Integration of a Solar Powered Unmanned Aerial Vehicle and a Wireless Sensor Network to Monitor Greenhouse Gases

Alexander Malaver ¹, Nunzio Motta ¹, Peter Corke ² and Felipe Gonzalez ^{3,*}

¹ Institute for Future Environments, School of Chemistry, Physics and Mechanical Engineering, Queensland University of Technology, 3 George St, Brisbane 4000, Australia;

E-Mails: alexander.malaverrojas@qut.edu.au (A.M.); n.motta@qut.edu.au (N.M.)

² School of Electrical Engineering, Computer Science, Robotics and Autonomous Systems, Queensland University of Technology, Brisbane 4000, QLD, Australia;

E-Mail: peter.corke@qut.edu.au

³ Australian Research Centre for Aerospace Automation (ARCAA), Queensland University of Technology, Brisbane Airport, QLD 4007, Australia

* Author to whom correspondence should be addressed; E-Mail: felipe.gonzalez@qut.edu.au; Tel.: +61-411-718-012.

Academic Editors: Vittorio M.N. Passaro and Fabrizio Lamberti

Received: 9 September 2014 / Accepted: 2 February 2015 / Published: 11 February 2015

Abstract: Measuring gases for environmental monitoring is a demanding task that requires long periods of observation and large numbers of sensors. Wireless Sensor Networks (WSNs) and Unmanned Aerial Vehicles (UAVs) currently represent the best alternative to monitor large, remote, and difficult access areas, as these technologies have the possibility of carrying specialized gas sensing systems. This paper presents the development and integration of a WSN and an UAV powered by solar energy in order to enhance their functionality and broaden their applications. A gas sensing system implementing nanostructured metal oxide (MOX) and non-dispersive infrared sensors was developed to measure concentrations of CH₄ and CO₂. Laboratory, bench and field testing results demonstrate the capability of UAV to capture, analyze and geo-locate a gas sample during flight operations. The field testing integrated ground sensor nodes and the UAV to measure CO₂ concentration at ground and low aerial altitudes, simultaneously. Data collected during the mission was transmitted in real time to a central node for analysis and 3D mapping of the target gas. The results highlights the accomplishment of the first flight mission of a solar

powered UAV equipped with a CO₂ sensing system integrated with a WSN. The system provides an effective 3D monitoring and can be used in a wide range of environmental applications such as agriculture, bushfires, mining studies, zoology and botanical studies using a ubiquitous low cost technology.

Keywords: air pollution monitoring; environmental monitoring; gas sensors; greenhouse gases; nanostructured metal oxide sensors; UAV; UAV; WSN; solar energy

1. Introduction

Large scale monitoring of gases produced by the environment, industry and agriculture is a demanding task that requires long periods of observation, large numbers of sensors, data management, high temporal and spatial resolution, long term stability, computational resources, and energy availability. WSNs and UAVs are a good alternative for such demanding tasks, although their development and availability is limited by factors such as sensor stability over long periods, energy availability when deployed in remote areas, payload weight for small Unmanned Aerial Vehicles (UAVs), management of data produced by sensor nodes, and cost.

Recent technological improvements in gas sensors, electronics, telecommunication, solar cells, and avionics have made possible the development of WSNs and UAVs equipped with gas sensing systems for high spatial and temporal resolution. Such systems have broad scientific and industrial applications including monitoring anthropogenic emissions of greenhouse gases (GHG) such as CO₂ [1,2], as well as local pollutants from bushfires, cities, factories, and agricultural fields such as NO₂ [3,4] and CH₄ [5–7]. Practical application of WSNs has been proposed for monitoring fugitive CH₄ emissions [6], coal fields or biomass degradation (landfills) [7], and NH₃ and N₂O gas releases from fertilizer use [8,9]. Some of these systems are already commercially available, but the cost/benefit ratio is still too high to be widely used. WSNs are essential to monitor large areas such as cities, roads, and forests due to their ability to communicate via nodes and multi hop data. These functionalities for example may allow the tracking and mapping of gas plumes to identify the plume origin at ground level.

UAVs can play an important role in environmental gas sensing in remote areas due to their capability to carry instruments, sensors and collect data with high spatial and temporal resolution [10,11]. UAVs have already been used to this purpose; for instance, Watai *et al.* [12] reported on the development of a non-dispersive infrared (NDIR) sensing system on a small UAV to monitor atmospheric CO₂ concentrations. The authors designed and built an economic and accurate gas sensor system (± 0.26 ppm precision) and performed several flight tests with a one hour flight autonomy and 3.5 kg payload. McGonigle, *et al.* [13] reported the measurements of volcanic gases with a helicopter UAV at La Fossa crater, Volcano (Italy), using an ultraviolet and infrared spectrometer to measure SO₂ and CO₂ gas concentrations. This UAV had a 3 kg payload weight and 12 min flight autonomy. Astuti, *et al.* [14,15] developed a fixed wing UAV for volcanic monitoring at Mt Etna. The UAV carried a CO₂ infrared spectrometer and an SO₂ electrochemical sensor. Khan, *et al.* [16] developed a greenhouse gas analyser using a vertical cavity surface emitting laser (VCSELs) embedded in a helicopter UAV. CO₂, CH₄ and

water vapour were targeted by developing a sensing module for each targeted gas, with a vertical and horizontal resolution of less than 1 m. Each module weighed 2 kg and required 2 W of power to operate.

The most popular gas sensing technology used in WSNs for environmental monitoring is based on Metal Oxide (MOX) resistive sensors, while optical gas sensing devices are more popular among UAV users [6,7,9,12,13,17]. This research aims at using the same sensing technology to integrate WSNs and UAVs in order to reduce complexity and cost. Both technologies were evaluated according to their advantages and disadvantages for ground and aerial mission; monitoring of continuous and instant release of pollutants; computational resources required; maximum achievable resolution; and financial cost. Table 1 presents a comparison of these two technologies.

Table 1. Advantages and disadvantages of MOX and optical gas sensing technologies when used in WSNs and UAVs.

Category	MOX Sensors		Optical Sensing Techniques	
	Advantages	Disadvantages	Advantages	Disadvantages
Aerial missions	Low energy consumption and light weight	Slow sensor response hinder aerial applications	Tested and proved	Energy consumption and weight may limit flight endurance
Ground missions	Tested and proven	Cross reference to different gases and sensitive to humidity	High sampling frequency, high specificity to target gas	No literature found, sensor are too expensive to be left unattended
Continuous release mission	Low energy and light weight, covers wide range of gases	No literature found	High sampling frequency, high specificity to target gas	Energy consumption and weight may limit flight endurance
Instantaneous release	Low energy and light weight, cover wide range of gases	Low sensor response time	High sampling frequency, high specificity to target gas	Energy consumption and weight may limit flight endurance
Computational resources	Few output variables, and same variables remain over large range of gases	No literature found -	No literature found	The number of output variables to measure depends on the optical technique used and target gas
Resolution	Regular resistive sensors achieve <i>ppm</i> resolution	Few sensors achieve <i>ppb</i> resolution	Several techniques achieve <i>ppm</i> and <i>ppb</i> resolution	No literature found
Cost position in Market cost	Low	None	NDIR modules have Low	Complex systems Medium to High

Recent advances in nanotechnology have benefited the development of MOX sensors facilitating the synthesis of novel classes of materials with enhanced gas sensing performance [18]. Within this nano-range, the physical, chemical, optical, mechanical, electronic and biological properties of these materials can be substantially different from those observed for the bulk sensing materials [18,19]. Such unique properties are attributed to the small size, as the quantum regime becomes predominant over the classical limit. The performance of nano-structured sensors depends also on the type of morphology. Research on 1-D nanostructures for gas sensing applications has intensified due to their high surface-to-volume ratio,

quantum confinement and improved crystallinity [20]. The most common 1-D metal-oxides nanostructures used in the fabrication of resistive based gas sensors are in the form of nanorods, nanowires, nanofibers, nanotubes, nanobelts, nanoribbons, nanowhiskers, nanoneedles, nanopushpins, fibre-mats, urchin, lamellar and hierarchical dendrites [21]. The MOX nanowires demonstrated improved sensitivity to a wide range of gas species and stability due to their high degree of crystallinity [22]. The increasing number of scientific publications focused on nanowires and nanowire based sensors during the last ten years reached its highest peak in 2011 [23]. The addition of a small amount of noble metals like Ag, Au, Pd, and Pt over the MOX surface; tuning of the working temperature toward a given compound with respect to another, coating the surface by specific functional groups can increase up to five times their sensitivity [24]; and multi-component sensing elements (sensor array) coupled with signal processing functions can be applied to differentiate the response of nanowires toward the target gas [22,25]. MOX sensors have found wide spread commercial applications [26], and most WSN users employed commercial MOX sensors. For the above mentioned reasons, this research selected MOX nanowires to measure CH₄ concentrations. Since optical sensing technologies have been widely tested for gas sensing applications and have produced high quality and reliable results [27] a NDIR sensor device was also selected to measure CO₂ concentrations.

Power is major issue for portable applications such as WSN and UAV because its availability limits their service life, reduces data collection and limits its applications. WSNs powered by solar energy have been developed [28,29], but their use for environmental gas sensing is limited. The concept of harvesting solar energy to power aircrafts in the field of UAVs has a long history and many solar powered aircraft have been successfully created [30,31]. The UAV developed in this work pursuit flight endurance and the ability to power a gas sensing system simultaneously. The following section describes the development of the gas sensing technology developed for the WSN and UAV.

2. Sensing System Design

2.1. Solar Powered WSN

The four principal components of our wireless sensor node are the Fleck [32,33], which is a microprocessor with networking capabilities, the humidity sensor, the solar panel with its power management electronics and the gas sensing system. The WSN was created by using the Fleck network cards developed by CSIRO [32,33]. The sensor board interface, microprocessor and communication capabilities of the sensor node were tested and reported in previous research papers [34–36]. Data collected from sensor nodes were stored and displayed on live webpages using the data management platform illustrated in Figure 1. The base node (Figure 2) was equipped with a Fleck and connected to the field computer by USB.

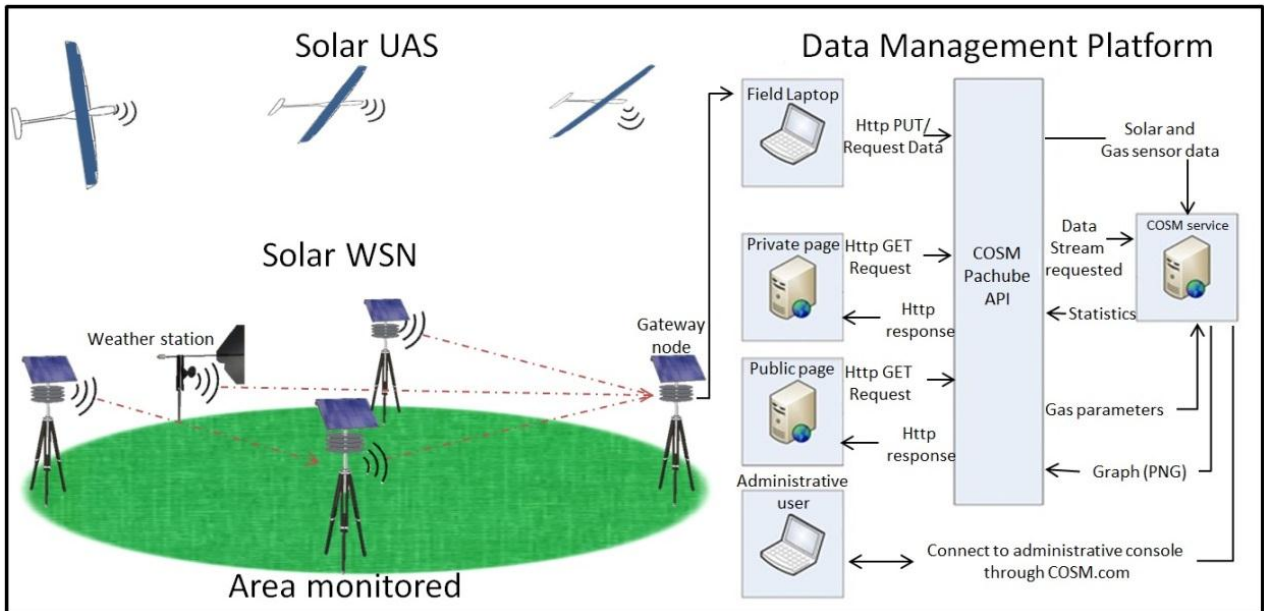


Figure 1. Illustrates the design of a solar powered WSN and a UAV integrated to a data management platform for continuous monitoring of pollutant gases.

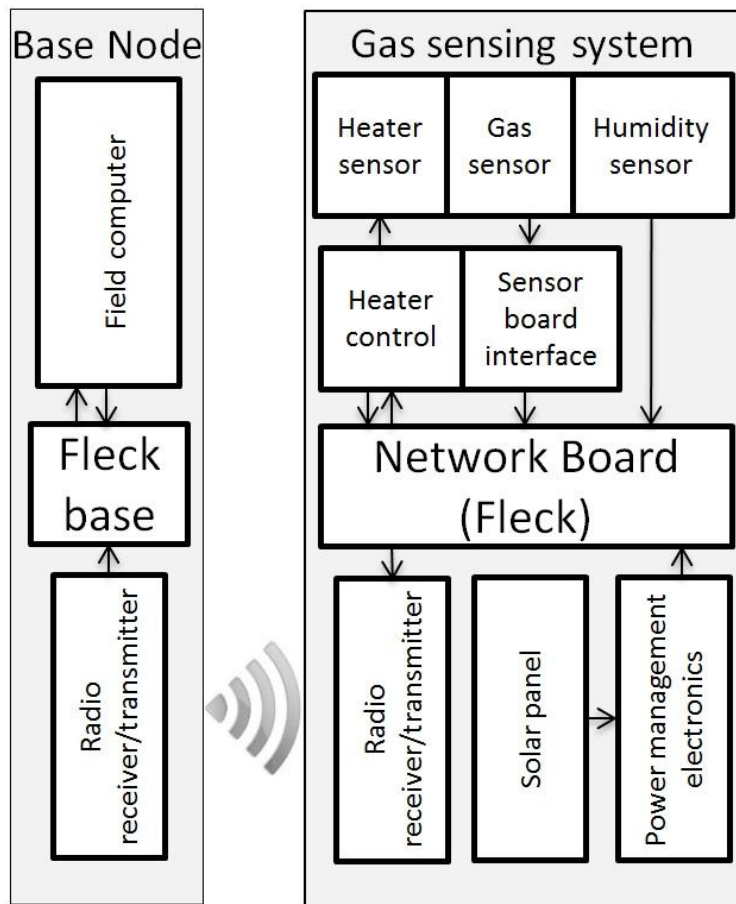


Figure 2. Wireless sensor node and base node configuration.

Humidity Sensor: humidity has an important influence on the performance of gas sensors, especially MOX sensors. Water absorbed on the MOX surface will not donate electrons to the sensing layers,

lowering the MOX sensitivity [20]. Prolonged exposure of sensors to humid environments leads to the gradual formation of stable chemisorbed OH^- on the surface causing a progressive deterioration of the performance of gas sensors [20]. Humidity interference is not expected in the SnO_2 sensor used for CH_4 samples, as the sensor temperature was higher than $200\text{ }^\circ\text{C}$, where molecular water is no longer present at the surface [37]. For this reason, the sensor node was equipped with a humidity sensor for studies where the sensor is kept at temperatures below $200\text{ }^\circ\text{C}$. A HIH-4010 humidity sensor from Honeywell Inc. (Minneapolis, MN USA) was selected as this sensor produces an output voltage ($\sim 0.8\text{--}3.8\text{ V}$) proportional and linear to the humidity percentage. The sensor board reads this signal using one of the ADC ports, and the data acquired is used to compensate any drift in the sensor baseline or sensor response, when the sensor works below $200\text{ }^\circ\text{C}$.

Solar Panel and Power Management: the power electronics manage the energy provided by the solar panel to supply regulated power to the sensor node ($3.5\text{--}6\text{ V}$, 500 mA), recharge a standard lithium battery (3.7 V , 1200 mAh) with the surplus energy, and keep the solar panel working at the maximum power point (MPPT). The BQ 24030 electronic chip from Texas Instruments Inc. (Dallas, TX, USA) [38] was selected and configured to develop this task, which bench testing and results were reported in previous published papers [34–36].

2.2. Gas Sensing System for the Wireless Sensor Network

MOX sensor: several MOX sensors developed by Brescia University and QUT (Queensland University of Technology) were tested at different CH_4 concentrations. Laboratory results indicated that a tin oxide (SnO_2) nanowire was the best candidate to be implemented in the WSN due to its appealing characteristic among the developed MOX sensors [25,39]. MOX sensors usually require working temperatures between $150\text{ }^\circ\text{C}$ and $400\text{ }^\circ\text{C}$ to activate the chemical reactions leading to the resistivity change when interacting with gases. The fabricated sensor has an embedded platinum heater at the back of the sensor plate. After several outdoor experiments, it was found that the sensor baseline drifted due to environmental conditions such as humidity and correlation to other gases [40]. A drifty baseline affects the reliability of the sensor measurements and requires re-calibration procedures. This undesirable effects increase substantially in aerial applications due to higher wind speed and variable atmospheric conditions.

In response to this challenge, a heating cycle protocol was developed to stabilize the sensor baseline for outdoor performance. The sensor heater was connected in series to a high frequency switching transistor and a shunt resistor to control and measure the delivered power. The transistor collector was connected to the positive power, the gate was connected to the Fleck and the Source was connected to the sensor. The power was provided by a fixed DC voltage (3.3 V), which was applied to the transistor. The opening and closing time of the transistor gate was controlled by the Fleck with a Pulse Width Modulation (PWM) signal, which regulates the heater current. The duty cycle of the PWM signal was adjusted automatically from 50% to 100% to reach the selected temperature based on the current measured on the shunt resistor, which is in series with the heater sensor. The heating cycle of the sensor was set to $300\text{ }^\circ\text{C}$ for 2.5 min, when exposed to CH_4 concentrations; and $400\text{ }^\circ\text{C}$ for 2 min in air, after each gas measurement to evaporate any water or gas molecule attached to the sensor surface, which produced a stable baseline.

MOX-CH₄ gas testing: the sensor response to CH₄ concentrations was evaluated at QUT laboratories by using a high precision multi-channel gas testing system. The testing system includes a 1100 cc test chamber capable of testing four sensors in parallel, eight high precision mass flow controllers (MKS 1479A, Andover, MA, USA) to regulate the gas mixture, 8-channel MFC processing unit (MKS 647C), and a picoammeter (Keithley 6487, Cleveland, OH, USA). The measurements were performed with a mixture of synthetic air and CH₄ gas at different concentrations (up to a maximum of 10.6 ppm of CH₄ balanced in synthetic air), 25 °C, and 0 humidity. The right concentrations of CH₄ gas in air were obtained by adjusting the respective flow rates via the MFCs, while maintaining a total constant flow rate of 200 SCCM (mL/min). The sensor heater was connected to an electronic board that executed the heating protocol described previously, and the picoammeter applied 1 bias volt to the sensor upon gas exposure in order to read the sensor resistance. The sensor was left in the test chamber overnight under dynamic flow of synthetic air, which helps to stabilize the sensing layer before the test. Once the sensor was stable, it was tested towards 5 and 10.5 ppm of CH₄ for 5 times in order to characterize the sensor response. The average time response (t_r) of the sensor was 15.7 min and 24.3 min, respectively when exposed to 5 ppm and 10.5 ppm of CH₄; and the average recovery time was 8.7 min at 5 ppm, and 8.86 min at 10.5 ppm. This sampling frequency will suit most of the studies required for ground pollutants, however this response time will hinder aerial applications that require faster responses. The sensor response can be expressed as the ratio of R_s/R_o , where R_s is resistivity in gas and R_o is the resistivity in air. R_s varied from 0 to 1.5, when CH₄ concentrations varied from 0 to 10.5 ppm, respectively (Figure 3). These values show that the sensor has high sensitivity to the gas for a short concentration span.

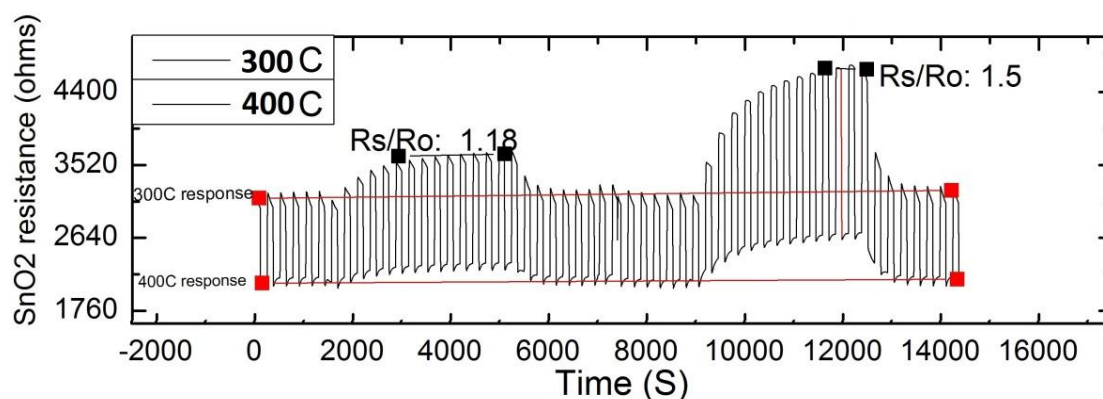


Figure 3. Response of the SnO₂ sensor for different concentrations of CH₄. The cycling temperature of the heater was 300 °C for 2.5 min and 400 °C for 2 min.

The sensor response exhibits a linear behavior for this short span concentration according to Figure 4. Therefore, the sensor response as a change in resistance was linearized to estimate concentrations from 0 to 10.5 ppm. The independent variable (gas concentration) was plotted on the X axis, while the dependent variable (estimated concentration) was plotted on the Y axis. A simple linear regression or least mean square (LMS) model was applied to the data in order to calibrate the system.

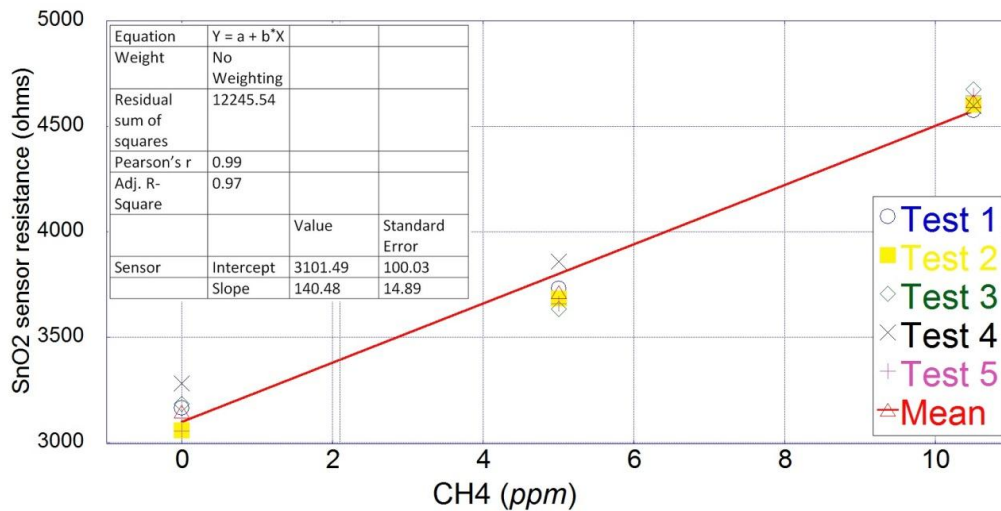


Figure 4. Linearization of the sensor response in resistance towards CH₄ concentrations from 0 to 10.5 ppm.

The intercept term (q) and slope parameter (m) were calculated using the following equations [41]:

$$Y = mX + q + \varepsilon \quad (1)$$

where m was calculated by using Equation (2):

$$m = \frac{(N \sum_i (X_i \times Y_i) - (\sum_i X_i) \times (\sum_i Y_i))}{N \sum_i (X_i)^2 - (\sum_i X_i)^2} \quad (2)$$

and q was calculated by using Equation (3):

$$q = \frac{(\sum_i Y_i) \times \sum_i (X_i)^2 - (\sum_i X_i) \times (\sum_i (X_i Y_i))}{N \sum_i (X_i)^2 - (\sum_i X_i)^2} \quad (3)$$

The variables are defined as:

- X: known gas concentration
- Y: sensor response in resistance (ohms)
- N: total experimental points
- i: sequence of each experimental point

By replacing the values on equation 1, the new estimated gas concentration (Y) values were defined as:

$$Y = 3101.4 + 140.48X \quad (4)$$

Field testing of the sensing systems: the baseline stability of the SnO₂ sensor was tested outdoors on the roof of S block at QUT, Gardens Point and at SERF (Samford Ecological Research Facility), QUT. The sensor was placed in a special sensor shelter powered by a solar panel. The temperature of the sensor was controlled by the heating protocol described in previous section, which results are plotted in Figure 5. Two sensor response levels are clearly identified from the graph in Figure 5. The bottom level was produced by the sensor response when heated for 2 min at 400 °C. This sensor response level was stable, with almost no drift and was used as sensor baseline. The top level response, produced when the sensor was heated for 2.5 min at 300 °C, is the sensor response towards environmental gases.

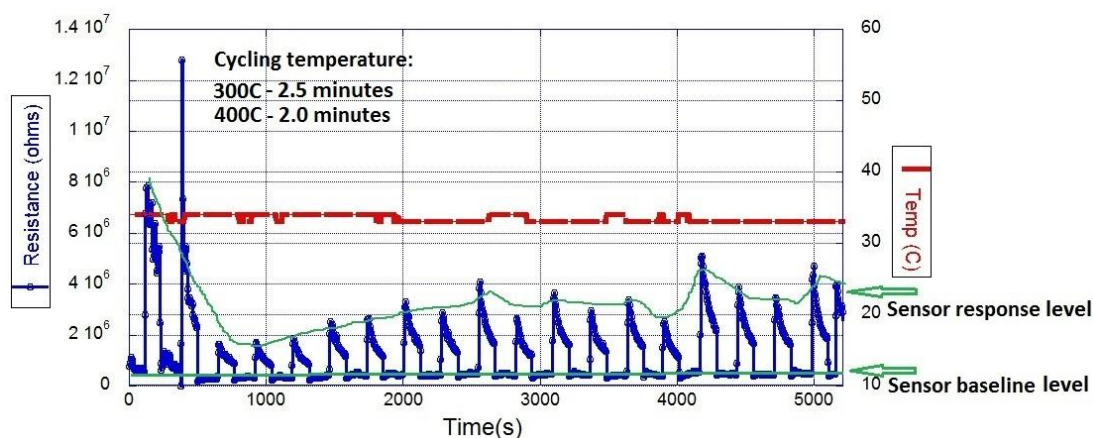


Figure 5. SnO₂ sensor response towards environmental gases in SERF, QUT, Brisbane, Australia.

CO₂ module: CO₂ concentrations were measured by an off-the-shelf NDIR sensor (CDM30K, Figaro Inc., Osaka, Japan), which is pre-calibrated from factory at 0 and 400 ppm. The accuracy of the reading were cross checked with a LI-840A CO₂ analyzer for one operational day showing an overall error in the measurements of 5%. The signal output of the module is a DC voltage between 0 and 4 V, which represents 0–2000 ppm, respectively [42].

The sensing system was tested under different environmental conditions in a farm field for 93 days. Figure 6 shows the CO₂ concentration and the temperature registered by one of the sensor modules during one day of operation. The CO₂ concentrations were mostly influenced by vegetation activity of the surrounded rural area, which increased the CO₂ levels during night periods and decreased it during sun-light hours. Conversely, the environmental temperature presented the opposite behavior. The carbon dioxide levels registered are similar to the values recorded by George *et al.* [43] in rural areas with extensive vegetation. Additionally, the output data was cross checked periodically with a CO₂ analyzer (Li-840A) to verify the reliability of the readings. Significant loss in performance was not detected during the time span of the experiment.

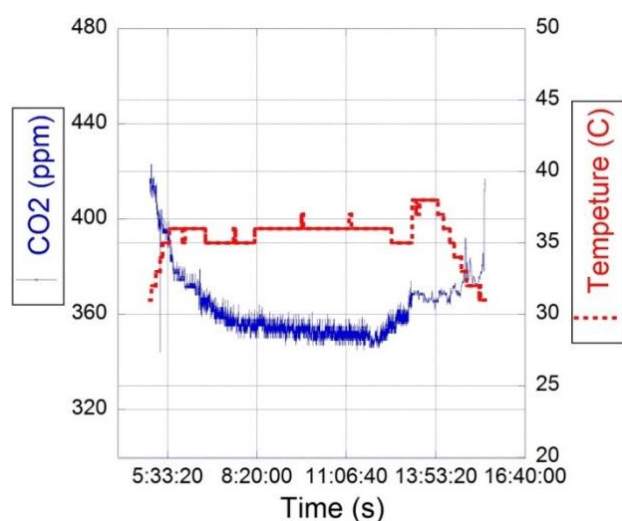


Figure 6. Response of one of the CO₂ nodes installed at SERF (QUT, Brisbane, Australia) during one day of operation.

2.3. Gas Sensing System for the Solar Powered UAV

The main sub-systems of the UAV are the gas sensing, navigation, communication, propulsion and power system, which are highly integrated into the aircraft frame. The block diagram of each sub-system is depicted in Figure 7. The Gas Sensing System described in Section 2.2 was installed in the UAV, and a sampling system was adapted to the sensor due to higher wind speed conditions. The main components of the system are the sensor, sensor heater, sensor board interface, a network board (Fleck) with radio transmitter/receiver capability and a solenoid valve control.

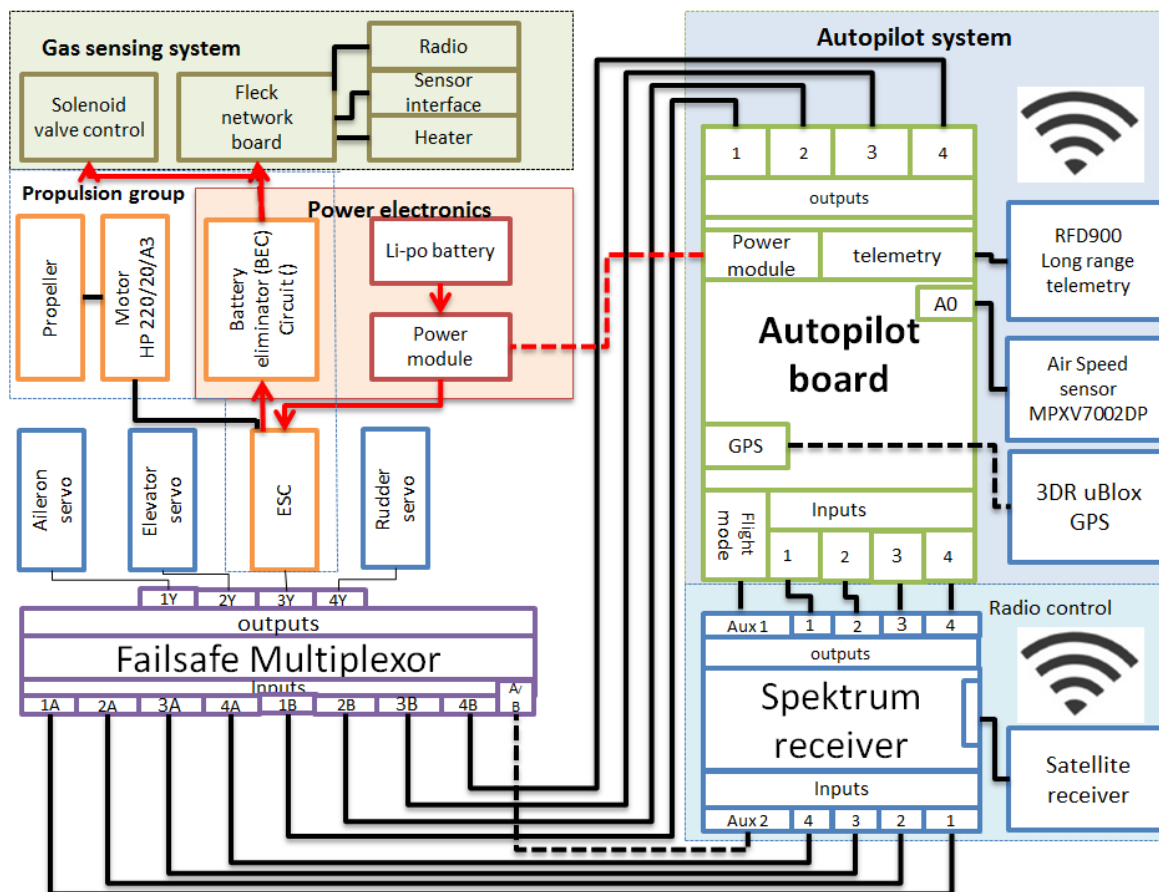


Figure 7. Configuration of the four main sub-systems integrated in the UAV.

The adaptations performed on the gas sensing system to make it functional for aerial missions are illustrated in Figure 8. The sample intake was adapted to capture samples for gas analysis during flight maneuvers. A fin shell was designed and 3D printed to house the gas sensing system on top of the central wing. The fin shell was made of lightweight materials (<50 g) to avoid significant drag and weight to the aircraft. A small gas chamber (63 cm³) was designed and installed inside the fin shell to retain the sample volume during analysis. The gas chamber has a T shape to let the sample flows across the horizontal trajectory and to insert the sensor in the vertical cavity, which ensures proper contact with the gas volume (Figure 8). A solenoid valve was installed at the inlet of the chamber to control the time and flow of the sample intake (Figure 8). The closing time of the valve depends on the sensor response time to the expected gas concentration, for instance 5 s close was enough time to analyze CO₂ concentrations from 0 to 400 ppm; and 2 s was the opening time of the valve to completely flush the chamber after each analysis.

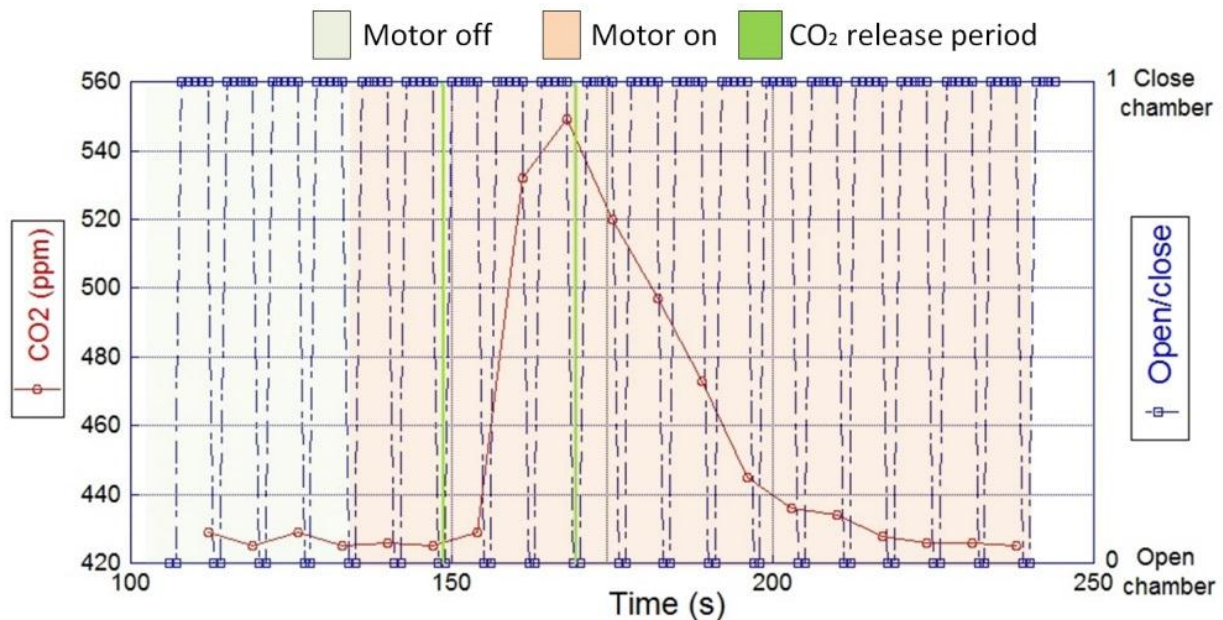


Figure 9. Bench testing of the CO₂ gas sensing system integrated in the aircraft fuselage.

Another bench testing was conducted to evaluate the performance of the CH₄ system integrated to the UAV. The development of the experiment was similar to the previously described CO₂ test; except for the valve control that was manually activated to determine the response time of the SnO₂ sensor. The testing procedure was developed as follows (Figure 9):

- First, the stability of the sensor baseline was verified with the avionics and motor of the aircraft switched off.
- Then, CH₄ emissions were released from a pollutant source in front of the UAV for 12 min, until the sensing system started to register changes in the sensor resistance.
- Next, the motor was switched on, clearing any remainder of emissions inside the chamber. It was observed that the sensor baseline dropped back to the resistance level registered at the beginning of the test.
- Emissions from a contaminant source were continuously released for 34 min at a rate of 1 L/min, while the motor was kept at 50% power.
- Once the emissions reached the gas sensing system, the solenoid valve was closed to fill the chamber with the gas volume, and let the sensor response to the gas concentration.
- After the sensor response was stable, the solenoid valve was re-opened for 2 s to flush the chamber, producing a sudden decrease in the sensor resistance.
- The previous procedure was repeated twice to verify the functionality of the solenoid valve and the sensor response to the contaminant.

The experiment successfully tested the performance of the gas sensing system during an emulated airborne operation, which results are plotted in Figure 10. The sensor baseline was stable under the regular wind flow produced by the natural atmospheric dynamics and when the propeller was activated during the experiment, indicating a noise free background of the system. After the chamber was closed the sensing system detected variations in the sensor resistance, which indicates a successful capture of the sample and a stable environment inside the chamber. The closing time of the valve allowed the sensor

to reach its chemisorption and physisorption stability on each measurement. When the solenoid opened the chamber, the sample was washed away producing a sudden decrease in the sensor resistance, until it reached its baseline level again. It was observed that the probability of detecting contaminants in front of the aircraft was increased due to the vortex effect of the propeller. This fact confirmed that the location of the gas sample intake was not negatively affected by the propeller, which on the contrary could have a beneficial effect.

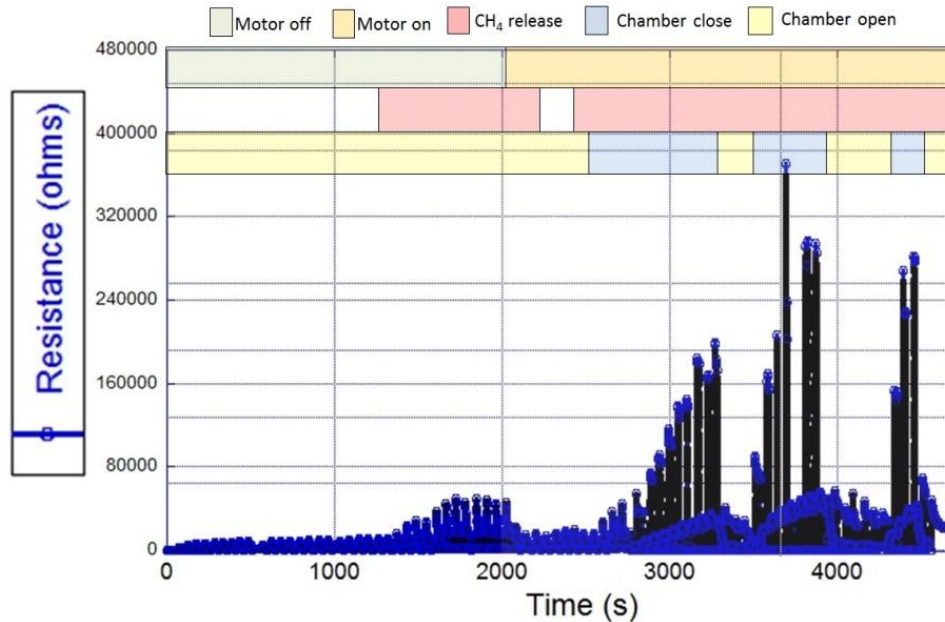


Figure 10. Bench testing of the CH₄ sensing system with a pollutant emission source.

3. Solar UAV Design and Flight Test

The UAV developed in this work was based on the Green Falcon UAV [44,45] developed at QUT and the Australian Research Centre for Aerospace and Automation (ARCAA). The principal sub-systems are: (i) Navigation system, which main components are the autopilot, air speed sensor, gyro sensor, accelerometer, magnetometer, barometric pressure, GPS, and fail safe system. The autopilot used in the UAV was the ArduPilot Mega 2.5, which is a complete open source autopilot system with a high benefit/cost ratio [46] and low weight (23 g). The autopilot system works mainly in three modes: autonomous mode, to fully perform unmanned mission by pre-programming waypoints from the ground control station (GCS). Stabilized mode, to assist a ground pilot in controlling and stabilizing the flight of the aircraft; in this mode the pilot has partial control of the aircraft and when there is no pilot input the autopilot will maintain a level flight of the aircraft. Manual mode, which is useful to perform the pre-flight check as the autopilot acts as a pass-through for all the RC commands; this mode allows the pilot to freely perform manual take-offs, maneuvers and landings, when the autopilot is not pre-programmed to perform these tasks. In all modes, the autopilot is capable of transmitting important flight information such as roll, pitch, yaw, airspeed, GPS position and battery status to the GCS by using the telemetry module.

The telemetry module used was the RFD900, which works at 900 MHz, is lightweight (50 g), small size, has large transmission range (>40 km), and requires about 1 W (+30 dBm) transmit power. The Mission Planner GCS was selected to create the waypoint mission based on Google maps, send

commands to the autopilot, receive and graph in real time autopilot’s data outputs, download mission log files, and data analysis.

The airframe is easy to transport for fast deployment and hand launched take off; it has a wingspan of 2.52 m, wing aspect ratio (AR) of 13, and length of 960 mm. The original weight of the wing was 960 g, and after the addition of the SSC panels it increased to 1610 g; therefore, the final weight of the UAV was 3285 g. (Figure 11A). The net power consumption of the UAV was 42.52 Wh, when equipped with the CO₂ sensing system (Figure 11B), and 42.92 Wh with the nano-sensor system. The pie chart evidenced that the power consumption of the gas sensing system was only a small proportion of the total energy demand; and the energy consumption does not vary significantly between the CH₄ and CO₂ sensing systems.

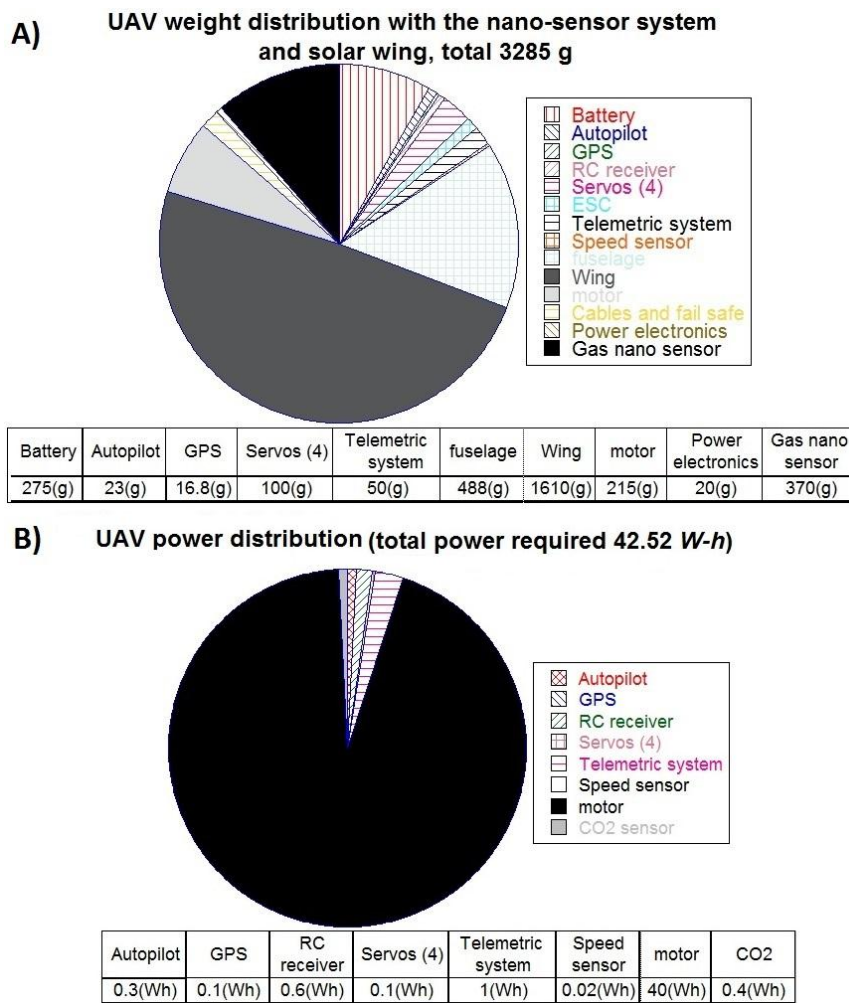


Figure 11. (A) Weight distribution of the UAV with the nano-sensor system; (B) power consumption breakdown of the UAV assembled with the CO₂ sensing system.

The total energy demand of the UAV is expected to be higher due to electronics inefficiencies that are calculated using Equation (5):

$$E_{demand_total} = \frac{(E_{avionics} + E_{gas_s})}{\eta_{power\ electronics} \times \eta_{avionics}} \tag{5}$$

where the efficiency of the power electronics (η_{pe}) is 0.86, and the avionics (η_{av}) is 0.90.

Replacing values in Equation (6):

$$E_{demand_total} = \frac{(42.12 Wh + 0.8 Wh)}{0.86 \times 0.9}$$

$$E_{demand_total} = 55.4 Wh$$

The total energy demand (55.4 Wh) needs to be supplied by the solar wing and the battery as follows.

The solar panels for the wing were constructed using small silicon solar cells (SSC) ribbons connected in serial and parallel configuration to achieve the voltage and current required. Each SSC ribbon has an area of 0.00375 m² and 12% efficiency. The solar panel area was limited by the wing area (490 cm²), ailerons, narrow ends, and the area allocated for the gas sensing system (53 cm²). Finally, 70 SSC ribbons were distributed along the available wing area (Figure 12), which output power produced was calculated as follows:

$$Area_{SSC_panel} = Area_{SSC_ribbon} \times 70 units = 0.2625 m^2 \tag{6}$$

The average output energy of the panels was calculated based on the mean sunshine hours of Brisbane (QLD, Australia), which are 7.4 h with a mean irradiance of 750 Wh/m², according to the Australian Bureau of Meteorology. Therefore, the expected average energy produced by the solar wing is:

$$Energy_{SSC\ panel} = \frac{0.2625 m^2 \times 750 Wh \times 0.12}{1 m^2} = 23.625 Wh \tag{7}$$

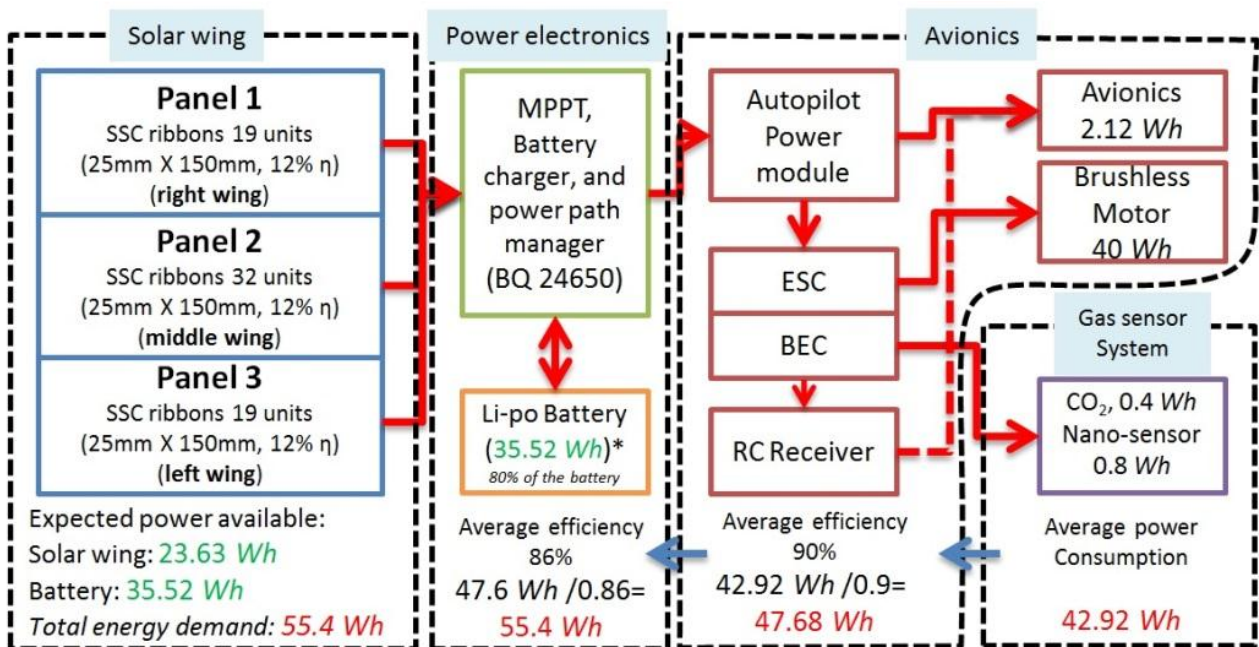


Figure 12. Energy demand and the energy available in the UAV.

A commercial lithium polymer 44.4 Wh, 3.0 mAh 4 cells battery was used in combination with the solar panel to meet the energy demand of the aircraft. Only 80% of the battery capacity (35.52 Wh) was taken into account for safety reasons. The total energy expected (Energy_{SSC panel} + Energy_{battery}) was therefore 59.14 Wh, enough to satisfy the total energy demand of the UAV. Figure 12 summarizes of the energy demand of the UAV and the energy available.

The SSC ribbons were distributed along the three parts of the wing by placing 19 units on each side wing (total 38), and 32 units in the middle wing for a total of 70 SSC units (0.2625 m^2). The weight density of a single SSC ribbon with the tabbing wire installed was 0.53 kg/m^2 , and the internal connections of panels were in serial configuration. The SSC panels were encapsulated in a flexible structure that takes the shape of the wing to avoid losses in aerodynamic performance and to withstand mechanical stress produced by the aircraft in operation. The encapsulation was developed by using a clear resin, which is flexible and totally transparent (Figure 13).

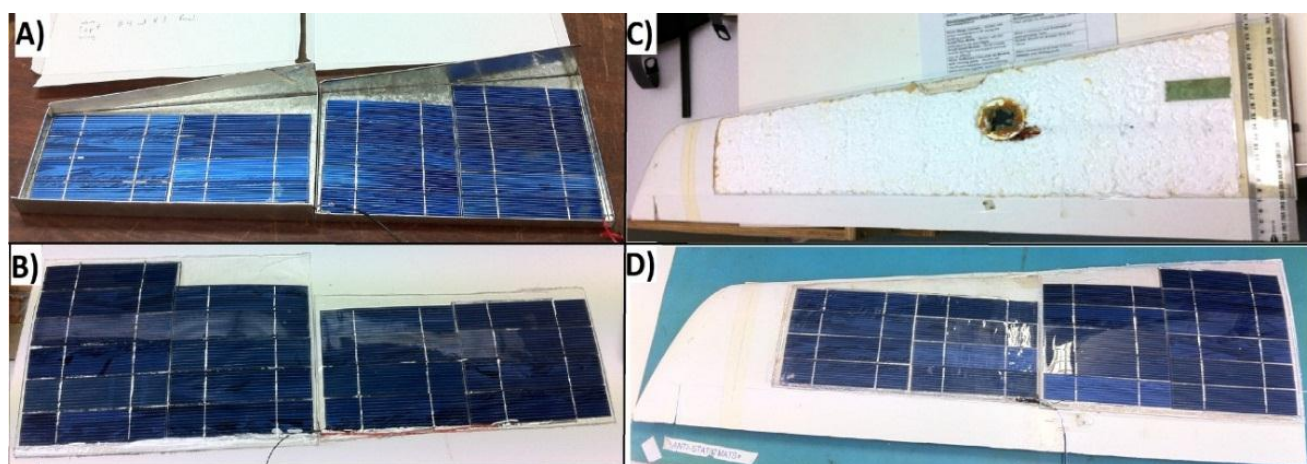


Figure 13. Solar powered wing construction: (A) left wing SSC panel in the mold; (B) right wing SSC panel encapsulated with clear and flexible resin; (C) left wing peeled on the skin to accommodate the solar panel; (D) final installation of the SSC panel on the surface of the wing.

The open circuit voltage (V_{oc}) of the side wing panels was $19 V_{oc}$, with an expected short circuit current (I_{sc}) of 1.16 A . The middle wing panel was constituted of 32 SSC ribbons in serial configuration, which produced $16 V_{oc}$, and short circuit current (I_{sc}) of 1.16 A (Figure 14). The right and the left wing panels were connected in series, and the output of these were connected in parallel to the middle wing panel in order to produce a final output of about $16\text{--}19 (V_{oc})$, $2 \text{ A} (I_{sc})$ (Figure 14). The panels have slightly different output voltage was due to space limitation in the wings; this fact is not desirable because it produces two different maximum power points and the panel with lower voltage becomes a load for the other. The problem can be solved by using two MPPT at the outputs, at expenses of increasing the power consumption and weight of the aircraft. For this reason, the solution implemented was to set the maximum power point of the MPPT in the middle of both output voltages (17 V) to mitigate this effect; this solution is viable due to the proximity of both output voltages. During flight operations is likely that part of the solar panel area is shaded due to flight manoeuvres; if this is the case, the shaded panel becomes a load for the others panels connected in parallel, or an obstruction for panels connected in series. A diode was installed at the output of each panel to create a bridge or a bypass to avoid this negative effect (Figure 14).

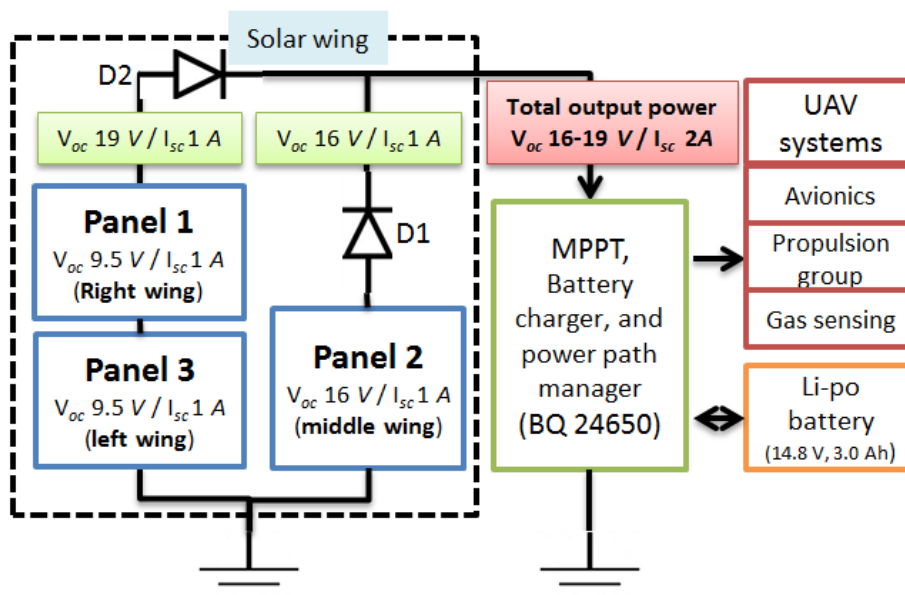


Figure 14. Panel configuration for the solar wing.

4. Field Testing of the Gas Sensing Technology and UAV

The first field test involved two nodes to monitor CO₂ at ground level, and the UAV equipped with the original wing (non-solar) to monitor CO₂ at about 100 m ASL. One ground node was connected to the base computer and the other solar powered node was located 30 m away, south of the ground station. The mission consisted of a continuous circular flight above the ground nodes for 20 min. The CO₂ readings recorded from the three sensors are shown in Figure 15. The geo-location of each sample was not reported in this experiment as the autopilot or a separate on-board GPS was not involved in the experiment. The graph shows that the ground node and the base node registered similar CO₂ concentrations of about 399 ppm throughout the test; the node located 30 m away showed some CO₂ spikes at the beginning of the test, corresponding to the emulation of a contaminant source. The aircraft readings are represented by the red line and their average value was 379.7 ppm. The readings from the UAV were slightly lower than the readings registered by the ground nodes, probably due to higher wind speed and slightly lower atmospheric pressure experienced during the flight mission. The values obtained are reasonable in comparison to the 392.722 ppm of CO₂ recorded by the Cape Grim Baseline Pollution Station (Tasmania, Australia), at the atmospheric baseline in June 2013.

The second test evaluated the solar powered wing and power electronics. The solar wing was installed on the aircraft and produced an open circuit voltage (V_{oc}) of 20.7 V, given the sun irradiance conditions of that day before the flight. The short circuit current (I_{sc}) was 2 A at full sun irradiance. The UAV was hand launched with the solar wing and the flight lasted for 20 min, showing a stable performance of both the aircraft and wing structure. Post-landing inspections did not show any significant deformation or structural failure of the solar panel or wing shape, indicating a successful construction technique for the solar wing. Figure 16 shows the final configuration of the solar UAV before the flight and an aerial photography of the aircraft flying.

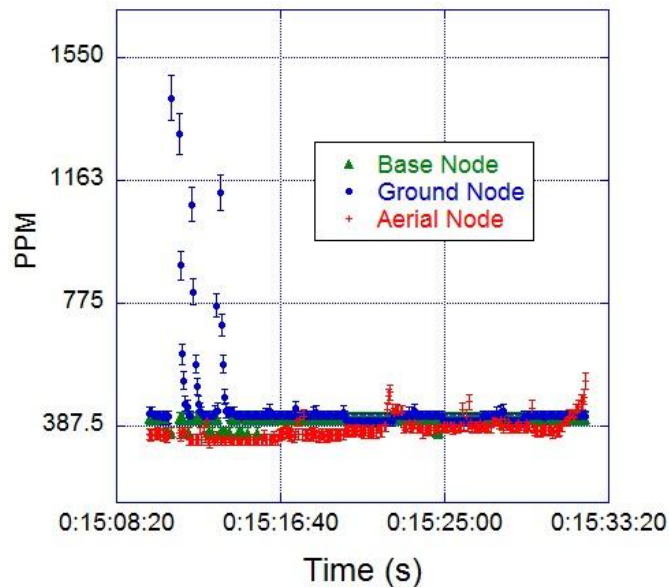


Figure 15. Monitoring of atmospheric CO₂ integrating two ground nodes and one aerial node.

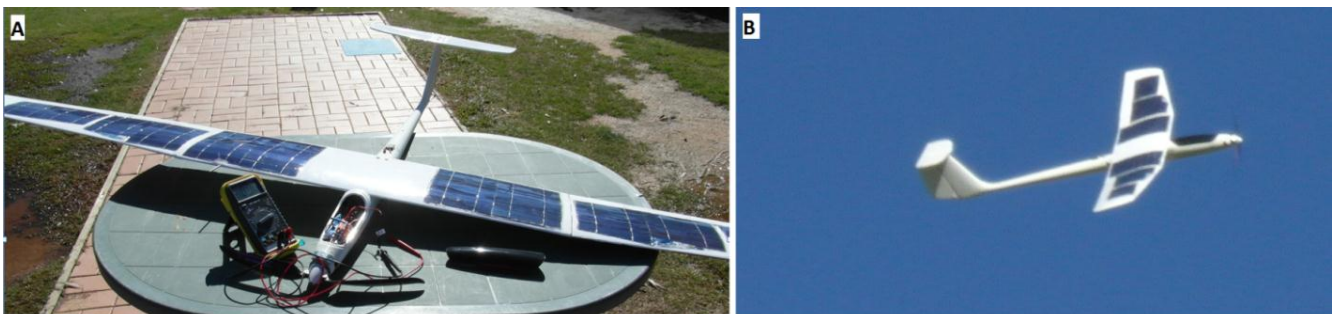


Figure 16. (A) Final configuration of the solar UAV; (B) aerial photography of the aircraft flying.

The final test integrated a GCS, a base node, one CO₂ ground node, a weather station, and the solar UAV equipped with a CO₂ node. The field test was developed in Christmas Creek, QLD on the 23 July 2013 and included the controlled release of a contaminant source. The CO₂ ground node and the weather station were deployed 20 m away, and the pollutant source 30 m away, south of the CGS. The mission of the UAV was to fly in a circular trajectory up to 50 m ASL over the area monitored, especially above the sensor node and pollutant source. The CO₂ contaminant was released for 6 min, at a rate of 0.0027 kg/s, for a total mass of 1 kg with an average wind speed of 1.09 m/s (Figure 18).

The flight operation lasted for 20 min, and the base node successfully collected data from the ground and aerial nodes simultaneously. Figure 17 shows that the average CO₂ concentration registered by the ground node was 404 ppm during the first 164 s; then, the concentration rose to an average value of 442 ppm when the contaminant was released. The average CO₂ concentration registered by the aerial node was 400 ppm during the whole test, with few CO₂ peaks above the average. The field experiment was designed based on Papanikolaou *et al.* [47] studies on short term release of CO₂ from the Kit Fox gas field experiments. Their simulations showed that release of CO₂ clouds from natural sources or Carbon Capture and Storage (CCS) places can reach concentrations higher than 100,000 ppm with volumes of more than 100 m³ in few seconds. In the UK, the limits of CO₂ work place exposure are 0.5% (5000 ppm) for long term exposure (8 h); 1.5% (15,000 ppm) for short term exposure (15 min); and 70,000–100,000 ppm for

instant exposure (>1 s), which represents immediate danger to human life or health. The proposed WSN and UAV are suitable to perform monitoring on previous scenarios where ground sensors can raise an early alarm that launches a UAV to monitor the evolution of the CO₂ cloud. The data collected will be invaluable for emergency service and control systems in order to evacuate affected areas and predict the evolution of the pollutant cloud.

Post-flight analysis on the data collected from the GCS logs indicated that the horizontal sampling resolution of the UAV was 88.2 m, based on the average cruise speed of 12.6 m/s and the sampling frequency of 7 s. The total volume monitored was 3×10^6 m³ based on the circular area travelled ($r = 140$ m) by the UAV and the flight altitude of about 50 m ASL. Figure 18 illustrates the area monitored by the UAV, where the origin of the circle represents the contaminant source and the area affected by the emissions is delimited by l , due to the wind effect. The wind was blowing constantly in the North-East direction during the test, creating a narrow corridor of about 40° (Θ) for the contaminant emissions.

Therefore, the maximum radius (r) of the monitored area was 140 m, with a maximum arc length of 97.7 m. This indicated that just one measurement was possible per circular flight on the affected zone due to the horizontal resolution of the UAV (88.2 m).

Geo-location of the sample was possible by synchronizing the log's time of the gas sensing board and the autopilot GPS before the mission started. The ability to geo-locate the sample and register the time allowed reconstruction of taken samples in three dimensions, which facilitates visualization of local concentrations and analysis. The data collected allowed the creation of contour maps that help to identify gradients of concentrations within the volume monitored. The CO₂ data values were interpolated based on Renka [48] and Yuan [49] algorithms used in OriginPro Graph processor program. The methodology creates contour maps in four steps: Triangulation, Linear Interpolation, drawing of contour lines and smoothing of the curves, based on the average flight altitude (50 m ASL), gas concentration, longitude and latitude coordinates of taken sample (Figure 19).

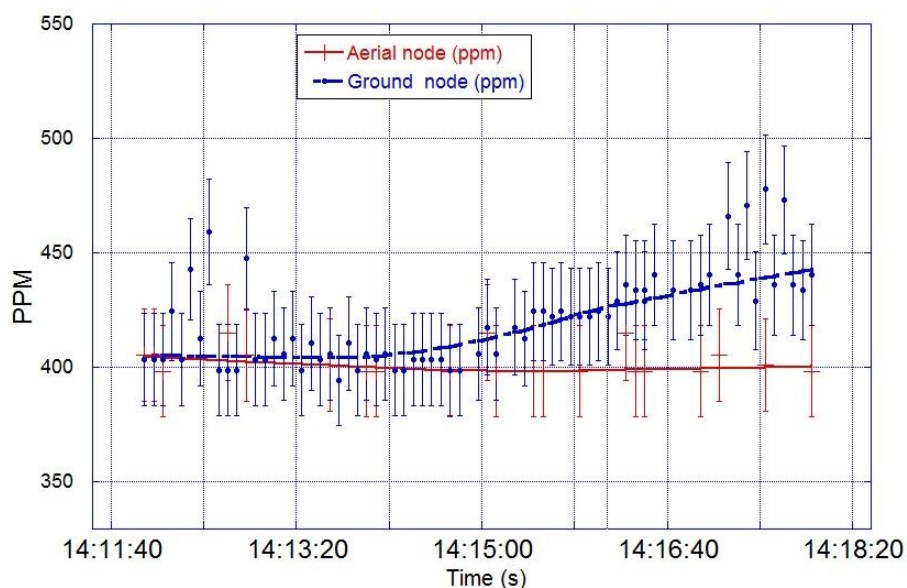


Figure 17. CO₂ readings from the ground node and aerial node during the field testing at Christmas Creek, QLD the 23 July 2013.

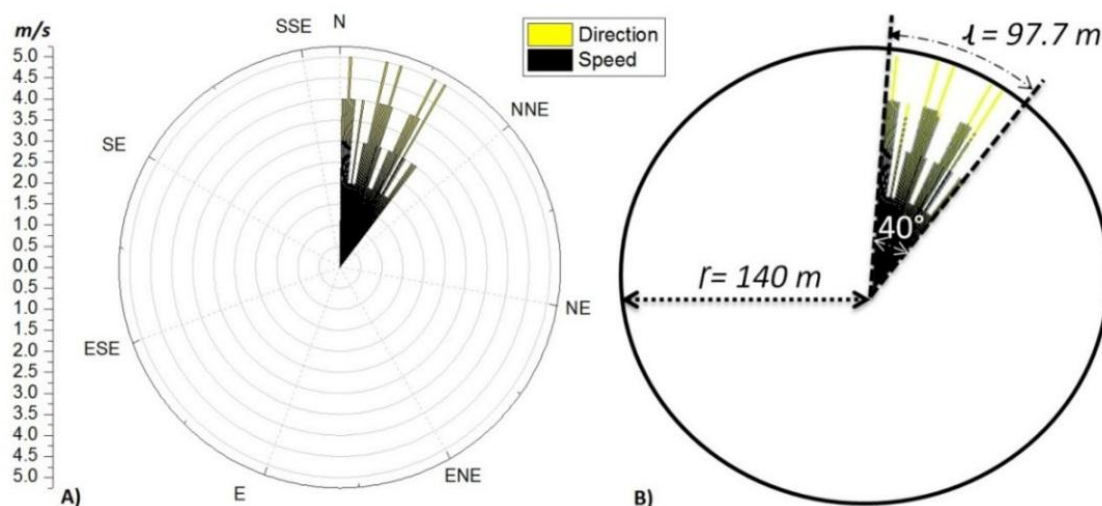


Figure 18. (A) Illustrates the direction and speed of the wind during the field testing; (B) illustrate the monitored area affected by the pollutant emissions due to the wind.

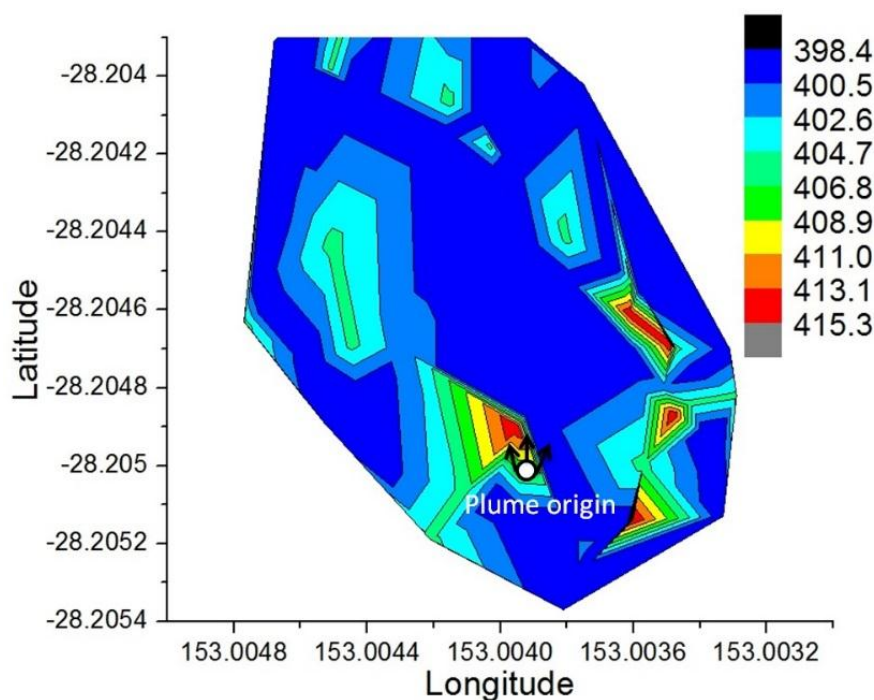


Figure 19. Contour map of the CO₂ concentration estimated by the UAV within the 3×10^6 km³ monitored.

A 3D map in Google Earth was created based on the geo-location of the taken samples. Figure 20 indicates the real position of the base node, ground node, pollutant source and the taken samples during the experiment. A video of the project development is online at the Green Falcon project channel [50].

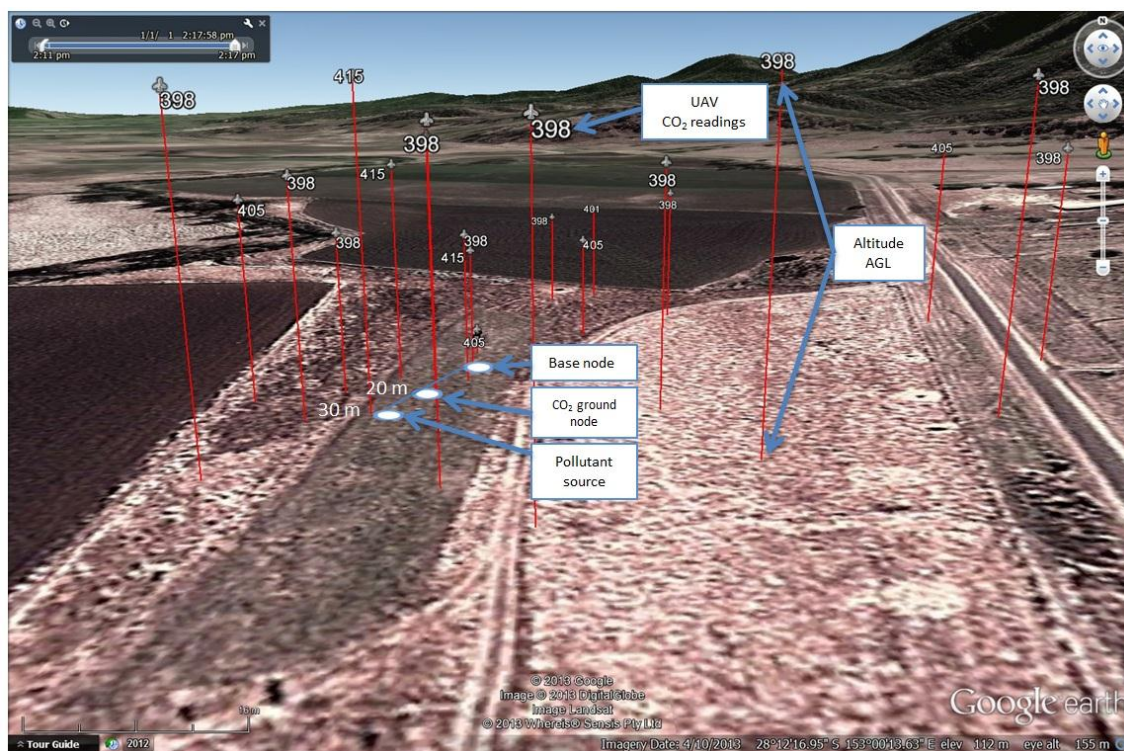


Figure 20. Geo-location and values of the CO₂ samples taken by the UAV during the field testing in Christmas Creek, 23 July 2013.

5. Conclusions

The WSN, UAV and gas sensing systems developed in this research are a response to challenges and limitations of WSNs and UAVs in the field of gas sensing and energy availability. The successful integration of a small solar powered aircraft equipped with a gas sensing system and networked with solar powered ground nodes proves the possibility of 3D monitoring of pollutant gases.

Our electric powered aircraft allowed the use of sensitive instruments and the execution of circular trajectories without self-contamination. A sensing system based on resistive MOX sensors was evaluated both for the WSN and the UAV. We addressed the problem of the drift baseline caused by environmental humidity and correlation to other gases by implementing a heating cycling protocol of the sensor. However, MOXs sensors were not used in flight operations due to their long response time that hinder aerial applications. Further research and development of MOXs nano-sensors is required to achieve the detection of single molecules of gas instantaneously [18]. Both our resistive gas sensing system and a commercial NDIR module were successfully adapted and tested for aerial missions, showing reliable performance and meeting the payload constraints of a small aircraft. A method to design, create and evaluate small solar powered UAVs equipped with a gas sensing system was successfully developed and validated with experimental testing.

The results are significant, as we believe that this prototype system is an important step for the future of environmental monitoring; and the advances in solar cells, batteries, and sensing technologies will open a wide market of intensive and capillary environmental data acquisition, not limited only to gas concentrations, but also to temperature, humidity, aerosols, pollens, *etc.*

Acknowledgments

The authors would like to acknowledge the financial support from the Queensland Government through the NIRAP project, “Solar powered Nano-sensors”. The collaboration of Fazl Alabodi, Mandeep Saini, Sarah Schaber, and Steven Bulmer. We would like to thank ARCAA for facilitating flight test activities and for their technical support. In addition, the authors acknowledge University of Brescia for providing MOX nano-sensors and Mahnaz Shafei for the use of the gas sensing facility and scientific advice.

Author Contributions

Alexander Malaver designed and realised the experimental set-up, built the solar wings, gas sensing system and conducted the experiments in the lab and on the field. He had the main role in the paper writing.

Nunzio Motta directed the sensing experiments and contributed in writing and proofreading the paper.

Peter Corke provided advice and technological guidance in the design of the Wireless Network System and contributed in revising the paper.

Felipe Gonzalez conceived the solar UAV project, directed the Unmanned Aircraft Vehicle modification and flight testing, and contributed in revising the paper.

Conflicts of Interest

The authors declare no conflict of interest.

References

1. Stocker, T.F.; Qin, G.; Plattner, M.; Allen, J.; Nauels, Y.; Bex, V. Climate Change 2013: The Physical Science Basis. Available online: <http://www.climatechange2013.org/report/> (accessed on 9 September 2014).
2. Climate Change 2007: Mitigation of Climate Change. Available online: http://www.ipcc.ch/publications_and_data/publications_ipcc_fourth_assessment_report_wg3_report_mitigation_of_climate_change.htm (accessed on 9 September 2014).
3. Frati, L.; Caprasecca, E.; Santoni, S.; Gaggi, C.; Guttova, A.; Gaudino, S.; Pati, A.; Rosamilia, S.; Pirintzos, S.; Loppi, S. Effects of NO₂ and NH₃ from road traffic on epiphytic lichens. *Environ. Pollut.* **2006**, *142*, 58–64.
4. Cape, J.N.; Tang, Y.; Dijk, N.V.; Love, L.; Sutton, M.; Palmer, S. Concentrations of ammonia and nitrogen dioxide at roadside verges, and their contribution to nitrogen deposition. *Environ. Pollut.* **2004**, *132*, 469–478.
5. Sihota, N.J.; Mayer, K.U.; Toso, M.A.; Atwater, J.F. Methane emissions and contaminant degradation rates at sites affected by accidental releases of denatured fuel-grade ethanol. *J. Contam. Hydrol.* **2013**, *151*, 1–15.
6. Tümer, A.E.; Gündüz, M. Design of a methane monitoring system based on wireless sensor networks. *Sci. Res. Essays* **2010**, *5*, 799–805.
7. Mitra, S.; Duttgupta, S.P.; Tuckley, K.; Ekram, S. Wireless sensor network based localization and threat estimation of hazardous landfill gas source. In Proceedings of 2012 IEEE International Conference on Industrial Technology (ICIT), Athens, Greece, 19–21 March 2012.

8. Jung, H.C.; Young, W.; Kyung, J.; Gi, J. Wireless electronic nose system for real-time quantitative analysis of gas mixtures using micro-gas sensor array and neuro-fuzzy network. *Sens. Actuators B Chem.* **2008**, *134*, 104–111.
9. Ruiz-Garcia, L.; Lunadei, L.; Barreiro, P.; Robla, J. A review of wireless sensor technologies and applications in agriculture and food industry: State of the art and current trends. *Sensors* **2009**, *9*, 4728–4750.
10. Sousa, J.B.D.; Goncalves, G.A. Unmanned vehicles for environmental data collection. *Clean Technol. Environ. Policy* **2010**, *13*, 369–380.
11. Gonzalez, F.; Marcos, P.G.; Castro, P.N.; Walker, R.; Zeller, L. Development of an autonomous unmanned aerial system to collect time-stamped samples from the atmosphere and localize potential pathogen sources. *J. Field Robot.* **2011**, *28*, 961–976.
12. Watai, T.; Machida, T.; Ishizaki, N.; Inoue, G. A lightweight observation system for atmospheric carbon dioxide concentration using a small unmanned aerial vehicle. *J. Atmos. Ocean. Technol.* **2005**, *23*, 700–710.
13. McGonigle, A.J.S.; Aiuppa, A.; Giudice, G.; Tamburello, G.; Hodson, A.J.; Gurrieri, S. Unmanned aerial vehicle measurements of volcanic carbon dioxide fluxes. *Geophys. Res. Lett.* **2008**, *35*, doi:10.1029/2007GL032508.
14. Astuti, G.; Giudice, G.; Longo, D.; Melita, C.D.; Muscato, G.; Orlando, A. An overview of the “volcan project”: An UAS for exploration of volcanic environments. In *Unmanned Aircraft Systems*; Valavanis, K., Oh, P., Piegler, L., Eds.; Springer Netherlands: Berlin, Germany, 2009; pp. 471–494.
15. Astuti, G.; Giudice, G.; Longo, D.; Melita, C.D.; Muscato, G.; Orlando, A. Hardware in the loop tuning for a volcanic gas sampling UAV. In *Advances in Unmanned Aerial Vehicles, State of the Art and the Road to Autonomy*; Valavanis, K.P., Ed.; Springer Netherlands: Berlin, Germany, 2007; pp. 473–493.
16. Khan, A.; Schaefer, D.; Tao, L.; Miller, D.J.; Sun, K.; Zondlo, M.; Harrison, W.; Roscoe, B., Lary, D.J. Low power greenhouse gas sensors for unmanned aerial vehicles. *Remote Sens.* **2012**, *4*, 1355–1368.
17. Berman, E.; Fladeland, M.; Liem, J.; Kolyer, R.; Gupta, M. Greenhouse gas analyzer for measurements of carbon dioxide, methane, and water vapor aboard an unmanned aerial vehicle. *Sens. Actuators B Chem.* **2012**, *169*, 128–135.
18. Kalantar, K.; Fry, B. *Nanotechnology-Enabled Sensors*; Springer Science & Business Media: Berlin, Germany, 2008.
19. Cao, G. *Nanostructures and Nanomaterials: Synthesis, Properties and Applications*; Imperial College Press: London, UK, 2004; p. 425.
20. Wang, C.; Yin, L.; Zhang, L.; Xiang, D.; Gao, R. Metal oxide gas sensors: Sensitivity and influencing factors. *Sensors* **2010**, *10*, 2088–2106.
21. Arafat, M.; Dinan, B.; Akbar, S.A.; Haseeb, A. Gas sensors based on one dimensional nanostructured metal-oxides: A review. *Sensors* **2012**, *12*, 7207–7258.
22. Soldano, C.; Comini, E.; Baratto, C.; Ferroni, M.; Faglia, G.; Sberveglieri, G. Metal oxides mono-dimensional nanostructures for gas sensing and light emission. *J. Am. Ceram. Soc.* **2012**, *95*, 831–850.
23. Comini, E. Integration of metal oxide nanowires in flexible gas sensing devices. *Sensors* **2013**, *13*, 10659–10673

24. Wang, H.T.; Kang, B.S.; Ren, F.; Tien, L.C.; Sadik, P.W.; Norton, D.P.; Pearton, S.J.; Lin, J. Hydrogen-Selective Sensing at Room Temperature with ZnO Nanorods. Available online: <http://scitation.aip.org/content/aip/journal/apl/86/24/10.1063/1.1949707> (accessed on 9 September 2014).
25. Comini, E.; Baratto, C.; Faglia, G.; Ferroni, M.; Ponzoni, A.; Zappa, D.; Sberveglieri, G. Metal oxide nanowire chemical and biochemical sensors. *J. Mater. Res.* **2013**, *28*, 2911–2931.
26. FIGARO. TGS 2444: For the Detection of Ammonia. Available online: <http://www.figaro.co.jp/en/product/entry/tgs2444.html> (accessed on 9 September 2014).
27. Hodgkinson, J.; Tatam, R. Optical gas sensing: A review. *Meas. Sci. Technol.* **2013**, *24*, doi:10.1088/0957-0233/24/1/012004.
28. Win, K.K.; Wu, X.; Dasgupta, S.; Wen, W.; Kumar, R.; Panda, S.K. Efficient Solar Energy Harvester for Wireless Sensor Nodes. Available online: http://ieeexplore.ieee.org/xpl/login.jsp?tp=&arnumber=5686355&url=http%3A%2F%2Fieeexplore.ieee.org%2Fxppls%2Fabs_all.jsp%3Farnumber%3D5686355 (accessed on 9 September 2014).
29. Alippi, C.; Camplani, R.; Galperti, C.; Roveri, M. A robust, adaptive, solar-powered WSN framework for aquatic environmental monitoring. *IEEE Sens. J.* **2011**, *11*, 45–55.
30. Noth, A. History of Solar Flight. Available online: <http://arc.aiaa.org/doi/abs/10.2514/6.1984-1429> (accessed on 9 September 2014).
31. Colella, N.J.; Wenneker, G.S. Pathfinder. Developing a solar rechargeable aircraft. *Potentials* **1996**, *15*, 18–23.
32. Sikka, P.; Corke, P.; Overs, L.; Valencia, P.; Wark, T. Fleck—A platform for real-world outdoor sensor networks. In Proceedings of Intelligent Sensors, Sensor Networks and Information, Melbourne, Australia, 3–6 December 2007.
33. Wark, T.; Corke, P.; Sikka, P.; Klingbeil, L.; Guo, Y.; Crossman, C.; Valencia, P.; Swain, D.; Bishop-Hurley, G. Transforming agriculture through pervasive wireless sensor networks. *Comput. Soc.* **2007**, *8*, 50–57.
34. Malaver, A.; Matteocci, F.; Carlo, A.D.; Corke, P.; Motta, N. Remote monitoring of outdoor performance of low scale dye sensitized solar cells for nanosensors nodes. In Proceedings of International Proceedings of Chemical, Biological & Environmental Engineering, Harbour Plaza Resort City, Hong Kong, 12 July 2011.
35. Malaver, A.; Corke, P.; Bell, J.; Depari, A.; Flammini, A.; Faglia, G.; Motta, N. Development of a gas nanosensor node powered by solar cells. In Proceedings of Solar2011, the 49th AuSES Annual Conference, Sydney, Australia, 2 December 2011.
36. Malaver, A.; Gonzalez, F.; Depari, A.; Corke, P.; Motta, N. Towards the development of a gas sensor system for monitoring pollutant gases in the low troposphere using small unmanned aerial vehicles. In Proceedings of Workshop on Robotics for Environmental Monitoring, Sydney, Australia, 19 July 2012.
37. Barsan, N.; Schweizer-Berberich, M.; Göpel, W.; Hesse, J.; Zemel, J.N. Fundamental and practical aspects in the design of nanoscaled SnO₂ gas sensors: A status report. *Fresen. J. Anal. Chem.* **1999**, *365*, 287–304.
38. Smith, N. Dynamic Power Path Management Simplifies Battery Charging from Solar Panels. Available online: <http://www.ti.com/lit/an/slua394/slua394.pdf> (accessed on 9 September 2014).

39. Comini, E.; Faglia, G.; Ferroni, M.; Ponzoni, A.; Vomiero, A.; Sberveglieri, G. Metal oxide nanowires: Preparation and application in gas sensing. *J. Mol. Catal. A Chem.* **2009**, *305*, 170–177.
40. Yu-Feng, S.; Shao-Bo, L.; Fan-Li, M.; Jin-Yun, L.; Zhen, J.; Ling-Tao, K.; Jin-Huai, L. Metal oxide nanostructures and their gas sensing properties: A review. *Sensors* **2012**, *12*, 2610–2631.
41. Leontitsis, A.; Pange, J. Statistical significance of the LMS regression. *Math. Comput. Simulat.* **2004**, *64*, 543–547.
42. FIGARO. CDM30K Carbon Dioxide Sensor Module. Available online: <http://www.figaro.co.jp/en/topic/2012/01/announcement-of-co2-gas-sensor-module-cdm30k.html> (accessed on 9 September 2014).
43. George, K.; Ziska, L.H.; Bunce, J.A.; Quebedeaux, B. Elevated atmospheric CO₂ concentration and temperature across an urban-rural transect. *Atmos. Environ.* **2007**, *41*, 7654–7665.
44. Gonzalez, F.; Glassock, R.; Dumbleton, S. Flying Spore Trap Airborne based Surveillance: Towards a Biosecure Australia. Available online: <http://eprints.qut.edu.au/47803/> (accessed on 9 September 2014).
45. Gonzalez, F.; Alsabban, W.; Walker, R.A. *Solar Powered UAV for Fire Prevention and Planning*; QUT: Brisbane, Australia, 2009.
46. Ardupilot-Mega. Available online: <http://plane.ardupilot.com/> (accessed on 9 September 2014).
47. Papanikolaou, E.; Heitsch, M.; Baraldi, D. Validation of a numerical code for the simulation of a short-term CO₂ release in an open environment: Effect of wind conditions and obstacles. *J. Hazard. Mater.* **2011**, *190*, 268–275.
48. Renka, R.J. Algorithm 623: Interpolation on the surface of a sphere. *Trans. Math. Softw.* **1984**, *10*, 437–439.
49. Yuan, F. Automatic Drawing of Equal Quantity Curve. Available online: http://en.cnki.com.cn/Article_en/CJFDTOTAL-JSFZ803.008.htm (accessed on 9 September 2014).
50. Malaver, A. Green Falcon UAV Final Test Campaign. Available online: <http://www.youtube.com/watch?v=aNmhM6XX5mE> (accessed on 5 November 2014).

© 2015 by the authors; licensee MDPI, Basel, Switzerland. This article is an open access article distributed under the terms and conditions of the Creative Commons Attribution license (<http://creativecommons.org/licenses/by/4.0/>).